Growth of complex volcanic ash aggregates in the Tierra Blanca Joven eruption of Ilopango Caldera, El Salvador

Henry Hoult[1*], Richard J. Brown[1], Alexa R. Van Eaton[2], Walter Hernandez[3], Katherine J. Dobson[4], Bryan Woodward[1]

[1]Department of Earth Sciences, University of Durham, Durham, DH1 3LE, UK
[2]U.S. Geological Survey, Cascades Volcano Observatory, Vancouver, Washington, 98683 USA
[3]Ministerio de Ambiente y Recursos Naturales, San Salvador, El Salvador
[4]Civil & Environmental Engineering, University of Strathclyde, Glasgow, G1 1XJ
*Now at: Earth and Environment, Beatrice Tinsley Building (Level 2), University of Canterbury, Private Bag 4800, Christchurch 8140, New Zealand
Corresponding author: henry.hoult@gmail.com

Abstract
Aggregation processes control both the residence time and dispersal of volcanic ash during eruptions yet remain incompletely understood. The products of aggregation vary from simple ash clusters to large, complexly layered accretionary lapilli. Here we detail the micro-stratigraphy of a single population of accretionary lapilli that grew during the ~431 CE Tierra Blanca Joven eruption from Ilopango Caldera, El Salvador. The accretionary lapilli were sampled 10 km from the caldera source within a sequence of ash-rich pyroclastic density current deposits and intercalated fall material, known as unit D, which is traceable >40 km from Ilopango. Scanning electron microscopy and image analysis reveal common facies that form distinct layers within the accretionary lapilli. Each facies is distinguished by quantitative and qualitative variations in particle size distribution, porosity, and particle fabric. We infer that these textures resulted from aggregation conditions that differed in terms of liquid water availability, particle concentration and grain size distributions. In our proposed model, a characteristic sequence of facies accreted from core to rim in the accretionary lapilli during passage through ash clouds generated by vent-derived plumes and pyroclastic density currents. The accretionary lapilli are mostly composed of smaller aggregates (ash clusters, ash pellets) and grew predominantly by accretion of already-formed aggregates, rather than by grain-by-grain accretion of individual particles. This finding is consistent with observations of rapid aggregate growth in volcanic plumes, suggesting a common evolutionary pathway for accretionary lapilli formation across diverse eruptions.

Keywords: Volcanic ash aggregates; accretionary lapilli; explosive eruptions; aggregation; volcanic ash; Phreatoplinian

1. Introduction

The aggregation of airborne volcanic ash particles during eruptions is an important control on ash dispersal through the troposphere and lower stratosphere (Carey and Sigurdsson, 1982; Textor et al., 2006). Aggregation can prematurely remove fine ash from eruption clouds by forming larger aggregates with greater terminal velocities than their constituent particles. Ash aggregation occurs within vent-derived eruption plumes and plumes rising above pyroclastic density currents (PDCs), also known as co-ignimbrite or co-PDC plumes (e.g., Gilbert and Lane 1994; Brown et al., 2010; Bonnadonna et al., 2002; Van Eaton and Wilson 2013). Aggregation processes depend on the energy of ash particle collision and sticking mechanisms (Iveson et al., 2001), such as electrostatic forces (e.g., Sorem 1982; James et al. 2002, 2003; Telling et al., 2013), hydrostatic bonds (Gilbert and Lane, 1994; Schumacher and Schmincke, 1995; Durant and Rose, 2009; Van Eaton et al., 2012a; Mueller et al., 2016), or ice sintering (Van Eaton et al., 2012a). Aggregation can result in increased ash loading in proximal regions, the generation of secondary thickness maxima, poor sorting, and reductions in ash concentrations in distal ash clouds (Sorem, 1982; Carey and Sigurdsson., 1982; Gilbert et al., 1991; James et al., 2002; Taddeucci et al., 2011; Wallace et al., 2013; Van Eaton et al., 2015).

A wide variety of volcanic ash aggregates fall from ash clouds, ranging from loosely bound particle clusters <100 μm in diameter, to complex, concentrically layered, sub-spherical balls >2 cm diameter (e.g. Carey and Sigurdsson, 1982; Sorem 1982; Schumacher and Schmincke, 1991; Bonadonna et al., 2002; Branney et al., 2008; Brown et al., 2010; Van Eaton et al., 2015). The most complex aggregates exhibit multiple internal layers and rims of 'ultrafine' ash, used here to indicate material predominantly <10 μm following Van Eaton and Wilson (2013). These complex accretionary lapilli (AP2 aggregates of Brown et al., 2012) are common in the deposits associated with pyroclastic density currents (e.g., Brown et al., 2010; Van Eaton and Wilson, 2013; Burns et al., 2017). Hypotheses for the formation of different layers within complex aggregates include variation in the sizes of particles available for aggregation (Gilbert and Lane, 1994; Schumacher and Schmincke, 1995) and variation in the amount of liquid water present during transport through distinct regions of the eruption cloud and associated ground-hugging currents (Brown et al., 2010; Van Eaton et al., 2012b, 2015; Durant and Brown, 2016; Mueller et al., 2016).

Here we provide a novel approach to characterizing the internal layers within complex accretionary lapilli. We analyse high-resolution 2D images collected by scanning electron microscopy (SEM) to quantify textural differences in the micro-stratigraphy of a population of ash aggregates taken from a single pyroclastic density current horizon of unit D from the Tierra Blanca Joven eruption (TBJ), which erupted from El Salvador's Ilopango caldera in ~431 CE (Hart and Steens-McIntyre, 1983; Pedrazzi et al., 2019; Smith et al., 2020; Brown et al., submitted). We elucidate aggregate growth history by relating internal stratigraphy to inferred processes in regions of the ash clouds and pyroclastic density currents and by reference to experimental studies of ash aggregation. The results are useful for investigating the range of conditions under which aggregation occurs in volcanic ash clouds, and particularly for determining if accretionary lapilli form by particle-by-particle, or by accretion of already-formed aggregates.

1.1 The Tierra Blanca Joven eruption, Ilopango Caldera, El Salvador

Ilopango caldera, El Salvador, is situated along the Central American Volcanic Arc, which stretches from Panama to Guatemala (Figure **1**; DeMets et al., 2010). The caldera itself is 8×11 km and hosts the long-lived Lake Ilopango. The distinctive Tierra Blanca Joven deposit (TBJ) represents the youngest explosive eruption from the caldera (Hart and Steen-McIntyre, 1983; Pedrazzi et al., 2019). It ranks as one of the largest Quaternary eruptions in Central America, with volume estimates in the range of 30–90 km^3 bulk (Dull et al., 2019). Several radiocarbon dates have been proposed for the eruption (410–535 CE, Dull et al., 2001; 539 CE, Dull et al., 2019), with ash shards found in Greenland ice cores agreeing with the earlier end of this range (431 ±2 CE, Smith et al., 2020). The TBJ consists of six main units (units A–F), comprising fall and pyroclastic-density-current deposits, some of which flowed >40 km from the caldera (Hart and Steen-McIntyre, 1983; Pedrazzi et al., 2019; Brown et al., submitted). Multiple TBJ units indicate a hydromagmatic origin (Pedrazzi et al., 2019) and intra-caldera lake sediments >43.6 ka precede the TBJ deposits (Mann et al., 2004) indicating the presence of a long-lived lake over the caldera. Modelling suggests the vent-derived eruption columns may have reached ~30 km high and co-PDC plumes associated with the final climactic phase may have reached ~50 km high (Pedrazzi et al. 2019). Ash was dispersed widely across the region

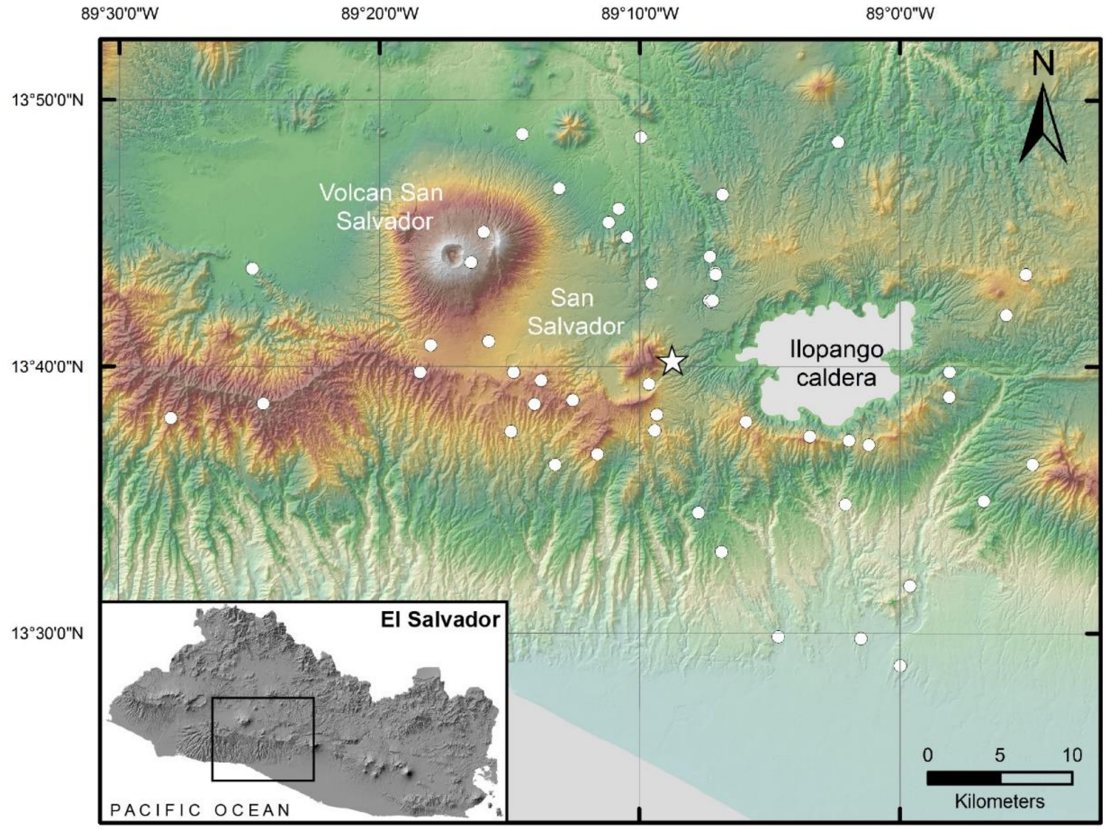

Figure 1. Map of the study area showing Ilopango caldera on the outskirts of San Salvador and location of measured sections of unit D of the Tierra Blanca Joven eruption deposits (white circles) from Brown et al. (submitted). The location of samples collected for this study is labelled with a star (locality 4: 13º39’21.41”N, 89º9’38.22”W). Inset shows location of study area within El Salvador.

now encompassing El Salvador, Guatemala, Honduras and Nicaragua, and out into the Pacific Ocean (Kutterolf et al., 2008; Pedrazzi et al., 2019).

The aggregates examined in this study were taken from unit D (Figure 2), which is a >6-m-thick succession of stratified, ash-rich pyroclastic-density-current deposits and intercalated thin, clast-supported ash-pellet fall layers (Brown et al., submitted). Accretionary lapilli are abundant in unit D and are both matrix and clast-supported throughout. Unit D is inferred to originate from Phreatoplinian activity involving extensive incorporation of lake water into the eruptive mixture based on its ash-rich, widely-dispersed, and heavily aggregated deposits that are depleted in lapilli-sized pumice (Walker, 1981; Self and Sparks, 1978; Brown et al., submitted). Pauses in pyroclastic density current activity allowed the fallout of ash pellets and accretionary lapilli (Brown et al., Submitted). Samples for this study were collected from a proximal locality ~10 km west of the caldera center (locality 4, shown as a star in Figure 1 and photo in Figure 2).

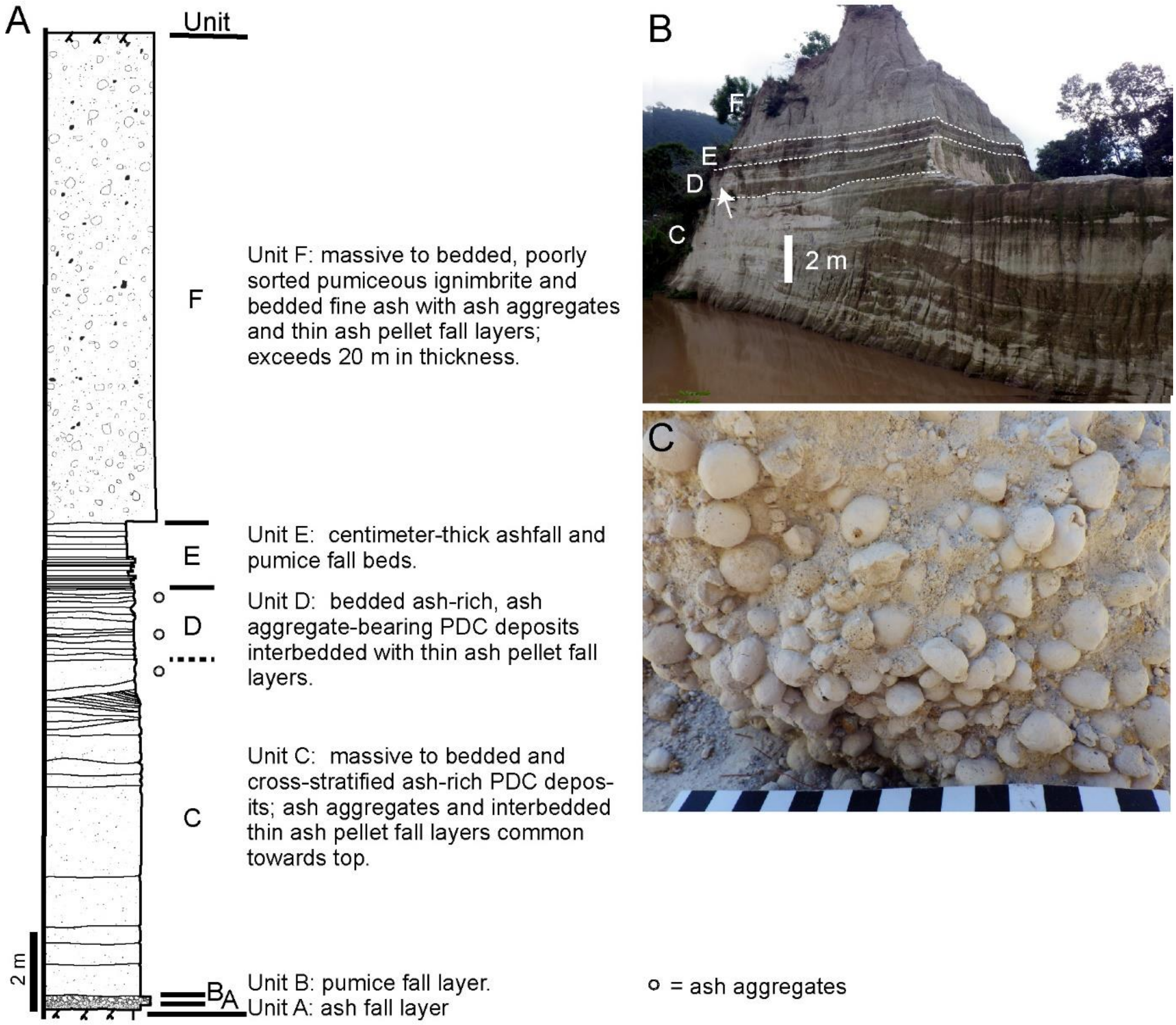

Figure 2. (a) Generalised stratigraphic section through the TBJ deposits, modified from Brown et al. (submitted). Adjacent circles represent the presence of aggregates. (b) Outcrop where accretionary lapilli samples were collected ~10 km from the caldera source (arrow). (c) Outcrop photograph showing the PDC-deposit-hosted accretionary lapilli. Scale in centimetres.

2 Methods

A sub-sample of 214 visibly intact accretionary lapilli were extracted from a bulk sample of unconsolidated unit D deposits (Figure 3; sampling location shown in Figs. 1–2). The aggregates were dried, weighed, photographed, and their long, intermediate, and short axes were measured using digital callipers. Density was obtained from dry mass and axes measurements. Fall velocity (w) was calculated as $w = C_d\ (d \cdot g \cdot \rho / \beta)^{1/2}$, where C_d=drag coefficient (taken as 1.054), d = equivalent spherical diameter, g = gravitational acceleration, ρ = measured aggregate density in kg m^{-3}, and β = air density at sea level (1.2 kg m^{-3}), as in Carey and Sparks (1986) and Van Eaton and Wilson (2013).

Figure 3. Photographs of exteriors of representative TBJ ash aggregates. Note the range in size and shape, especially the presence of exterior lumps (example highlighted by arrow).

Nine aggregates representative of the full range of sizes and shapes of the sampled population were made into polished thin-sections and imaged using a Hitachi SU70 Scanning Electron Microscope. Backscatter images were acquired at magnification of 120x using an automated stepwise grid collection programme in Oxford Instruments' Aztec software. The images were montaged using ImageJ's Stitching plugin, permitting qualitative analysis of their interior structures. Two aggregates (samples #2 and #21) that had complex, yet different, internal structures were selected for quantitative facies analysis. Structural and particle characteristics for these two aggregates were collected using six full-diameter image traverses at 250x magnification. Each 1020 x 704 pixel (1 pixel = 2.5 µm) image was divided into five 204 x 704 pixel regions for analysis. This encompassed as large an area as possible (1.84 mm = the largest measurable particle length) while only containing one facies per analysed region where possible. Textural variations between facies could then be distinguished.

Greyscale SEM images were segmented into binary images in Avizo 9.5®, (ThermoScientific™) using manually adjusted thresholds to highlight the details of porosity, particle shape and size. A separation algorithm enabled Feret-shape analysis of single particles (defined by pixel-face to pixel-face contacts). Feret shape is the ratio between the longest diameter and the shortest diameter orthogonal particle length. Mean particle length (M_z) and sorting (inclusive graphic standard deviation, σ_i) were calculated using Folk and Ward (1957) parameters in the R programming environment (see supplementary material). Uncertainty in these length measurements is approximately +/- 0.5 pixels (1.25 µm). Sorting classifications for σ_i values assume that 0.35–0.50 = well sorted, 0.50–1.00 = moderately sorted and 1.00–2.00 = poorly sorted after Folk and Ward (1957). Porosity was calculated using the Avizo Area Fraction module.

Particle clustering was visually identified as groups of particles surrounded by roughly equal-sized regions of angular pore space. Fabric was also visually defined – as a predominant alignment of the long axis of particles within an image. In regions of strong visual fabric, particles align concentrically (perpendicular to aggregate radius at a given point).

3 Results

Of the 214 TBJ aggregates measured in this study, most are spheroidal, but range from oblate to prolate (Figure 4). They range in maximum diameter from 7.5–27 mm, with a mean maximum diameter of 14 mm (Figure 3). About 20% exhibit prominent exterior lumps, each 1–4 mm in diameter (example shown in Figure 3). Larger aggregates tend to be lumpier. The density of the aggregates ranges from 0.7–2.3 g/cm^3 +/- 0.2 g/cm^3 (mean density 1.4 g/cm^3;

Figure 5). Terminal fall velocities, calculated by assuming dry aggregate density, range from 9–17 m s^{-1}.

Ash particles in the aggregates vary in shape from: (a) equant to tabular, (b) needle-like, angular, vitric ash, to (c) complex bubble wall shards (Table 1; Figure 6). Many ash particles contain whole or partial vesicles (Figure 6a). Subordinate oxide and feldspar crystals are usually either partially or completely enclosed in glass. Sub-rounded lithic ash particles, >200 µm in diameter, of mudstone, diatomite (Figure 7) and volcanic rocks are present in low abundances. A clay mineral matrix of unknown composition partially fills the pore space of most aggregates, as well as that of the host PDC deposit. It typically accounts for 5–10% of aggregate volume, increasing to 10–20% within the rims.

3.1 Internal facies of the aggregates

The nine aggregates studied in detail are composed of layers with distinct particle-size distributions, particle fabrics, and structures. These characteristics define three facies and two sub-facies.

3.1.1 Porous, clustered fine ash (pcA)

The porous, clustered fine ash facies (pcA) is characterised by a clast-supported framework of ash clusters (PC1 aggregates of Brown et al., 2012), each ~20–60 µm in diameter (Figure 6a). The clusters each consist of several tens of clast-supported ash particles. Maximum particle size is ~1.1 mm, mean particle lengths (Mz) are ~5 phi (23 µm; Table 1) with σ_I values of ~1 phi. Porosity values are ~30 vol. % and most pore space occurs between ash clusters (Figure 6a). There is no apparent particle fabric.

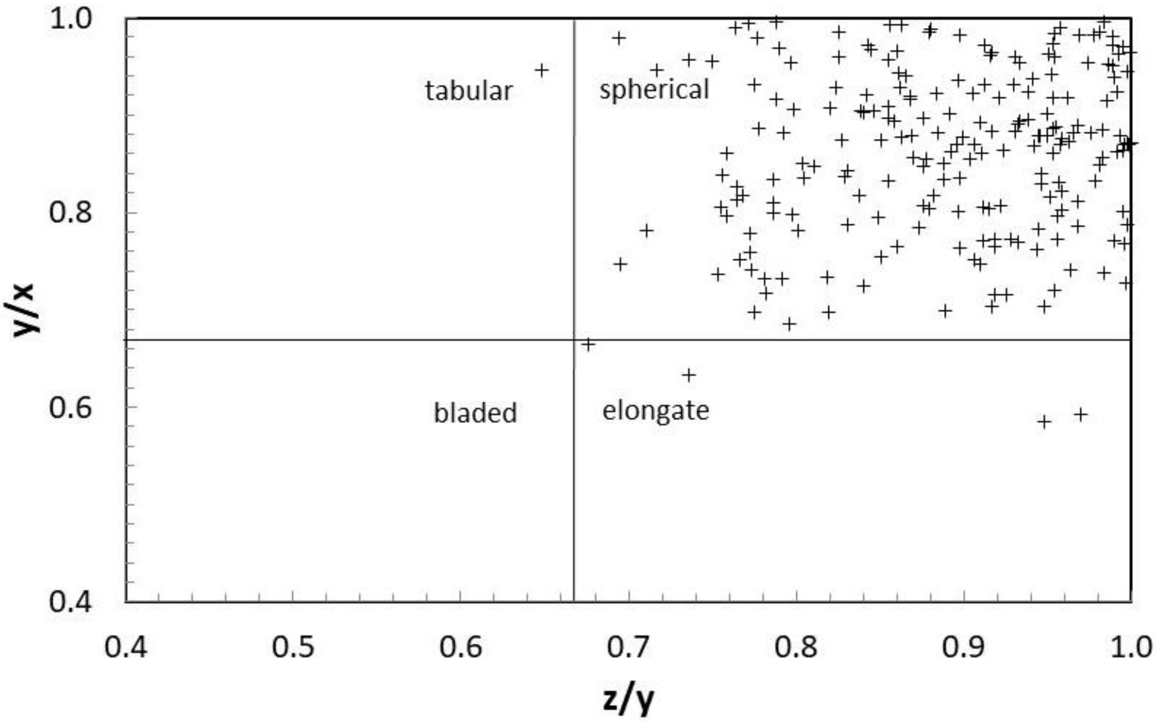

Figure 4. Partial Zingg plot (Zingg, 1935) of TBJ ash aggregates showing their predominantly spherical 3D shape (n=214); x = long axis, y = intermediate axis and z = short axis.

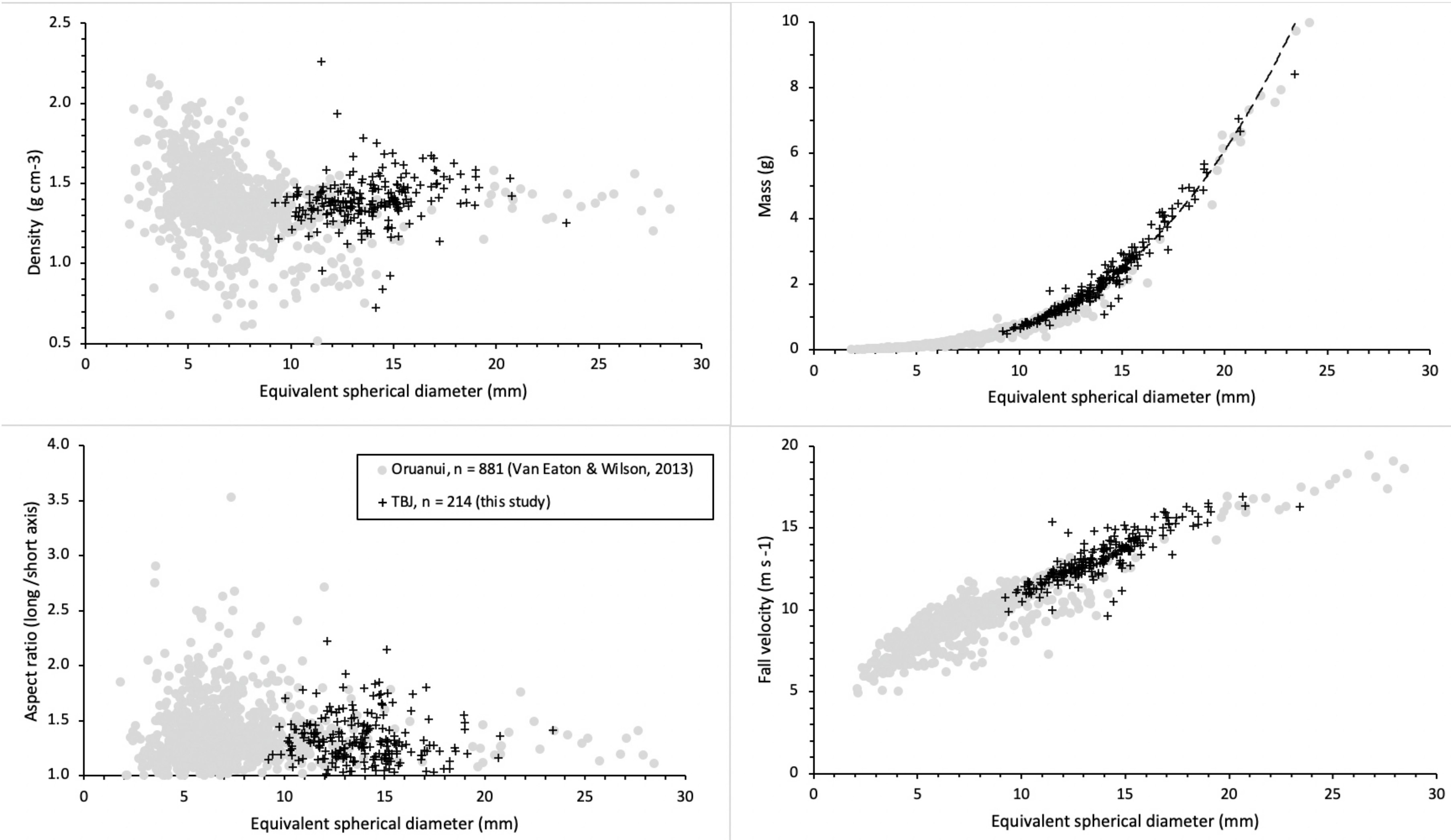

Figure 5. Physical characteristics of TBJ ash aggregates (n=214), in context with analogous examples from the Oruanui eruption of Taupo volcano, New Zealand, from Van Eaton and Wilson (2013), giving: (a) dry density, (b) aspect ratio, (c) dry mass, and (d) terminal fall velocity versus equivalent spherical diameter.

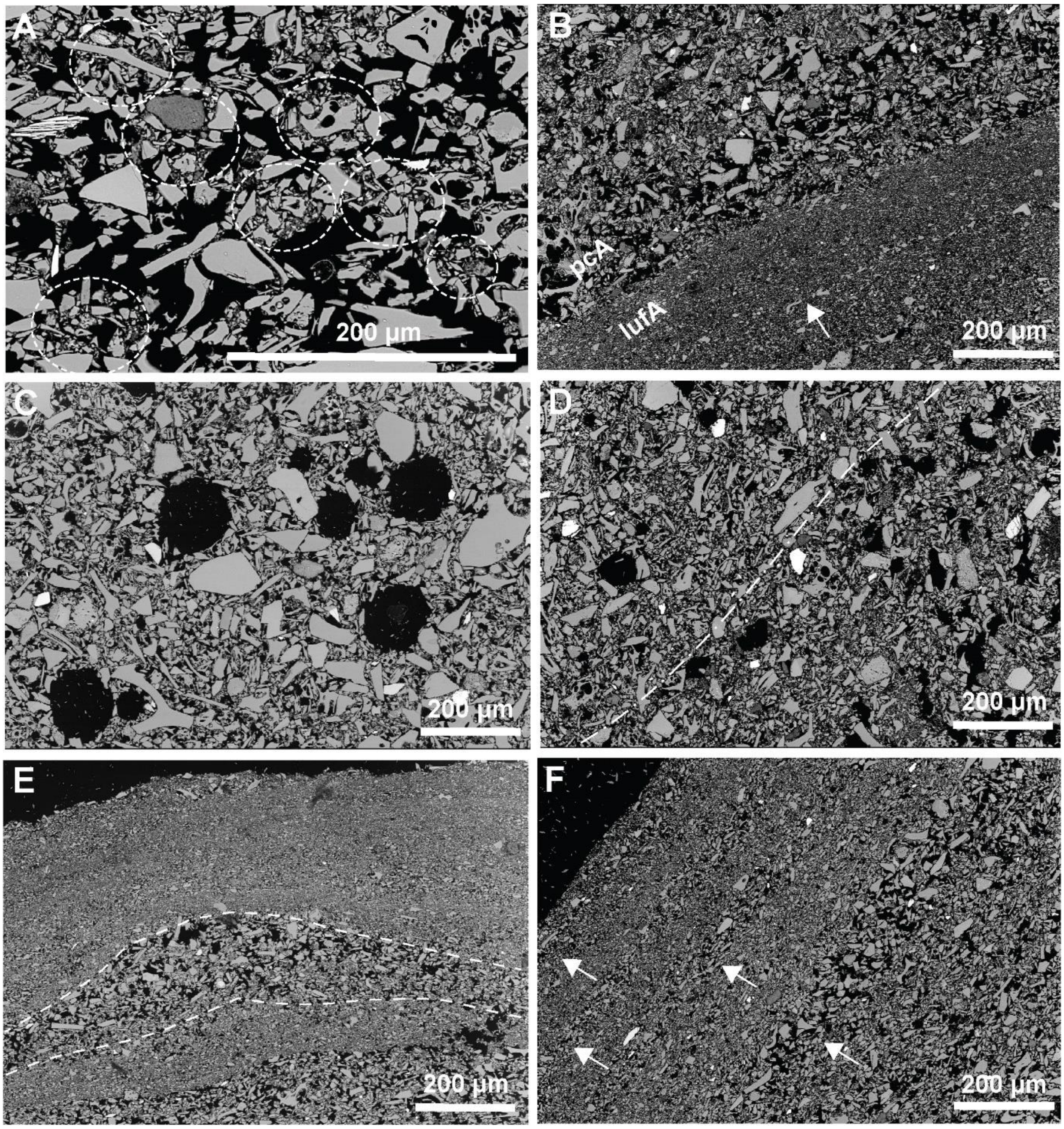

Figure 6. Backscatter SEM images of key features in the accretionary lapilli. (a) Ash clusters (circled) in porous, clustered ash facies (pcA). Clusters are recognisable by the presence of very fine ash particles between larger particles. (b) Contact between fine-grained rim (facies lufA) of early-formed recycled aggregate and porous, clustered ash facies (pcA) surrounding it. Arrow indicates discontinuous coarser-grained lamination. (c) Subspherical vesicles in layer of poorly sorted, massive ash facies (mA). (d) Contact between region of loosely packed fine ash, bottom right, within a region of poorly sorted, massive ash facies (mA), top left. (e) Coarse-grained lens in ultrafine grained rim (lufA). These are interpreted as small ash pellets that accreted to the exterior of the growing aggregate. (f) Ultrafine grained rim (lufA) showing detail of thin, coarser-grained laminations. Arrows indicate coarser-grained laminations. See Table 1 for facies descriptions.

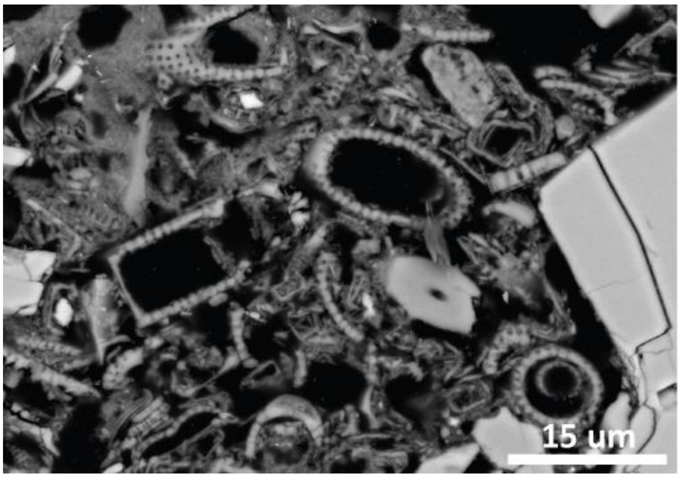

Figure 7. Backscatter SEM image of a clast of diatomite within a region of massive, poorly sorted fine ash (mA) in one of the accretionary lapilli.

The porous, clustered, laminated fine ash sub-facies (pclA) is composed of layers of ultrafine ash within layers of pcA. Each layer is <100 μm thick, and either pinches out laterally or truncates against other layers (e.g., Figure 8, S2). Elongate particles > 30 μm in diameter show moderately strong concentric fabric.

3.1.2 Massive fine ash (mA)

The mA facies is apparently structureless and lacks the ash clusters seen in the facies pcA. A distinctive feature of this facies is the presence of 2–5 vol % of larger ash particles and crystal fragments, each up to several-hundred microns in diameter (Table 1; Figure 8). Maximum particle length is 1.83 mm, mean particle lengths (M_z) are ~5 phi (26 μm) with σ_i values of ~1.2 phi. Particle size and σ_i values are considered lower estimates because the largest ash grains commonly exceeded the field of view during analysis (1.83 mm is the largest measurable value). Another distinctive feature are sub-spherical vesicles, <150 μm in diameter, which occur randomly distributed throughout this facies or arranged in crude layers (Figure 6c). Porosity is ~20 %. This facies visually shows no preferential particle orientation (Table 1).

The porous fine ash sub-facies (pA) is distinguished from the massive fine ash facies by the abundance angular interconnected pores <200 μm in diameter (e.g., Figure 8, S21). Particles >20 μm diameter show a weak concentric fabric. Fragments of ultrafine ash rims are occasionally present within layers of pA (e.g., Figure 8, S9).

3.1.3 Laminated, ultrafine ash (lufA)

The lufA facies is characterised by a homogenous, fine grainsize and strong layer-parallel orientation of elongate particles of all sizes (Figure 6f; Table 1). It typically forms the outermost layer of most aggregates (see Figure 6e–f) and is predominantly composed of ash particles <10 μm in size; particles larger than 60 μm are rare. Maximum particle length is ~370 μm, mean particle lengths (M_z) are ~6 phi (20 μm) with σ_I values of ~0.9 phi. While the SEM images used in this study resolved only particles >2.5 μm in diameter (the size of one pixel), laser diffraction analysis of aggregate rims from the same population (Brown et al., submitted) produces comparable Mz values (~6 phi) indicating few ash particles <2.5 μm were excluded.

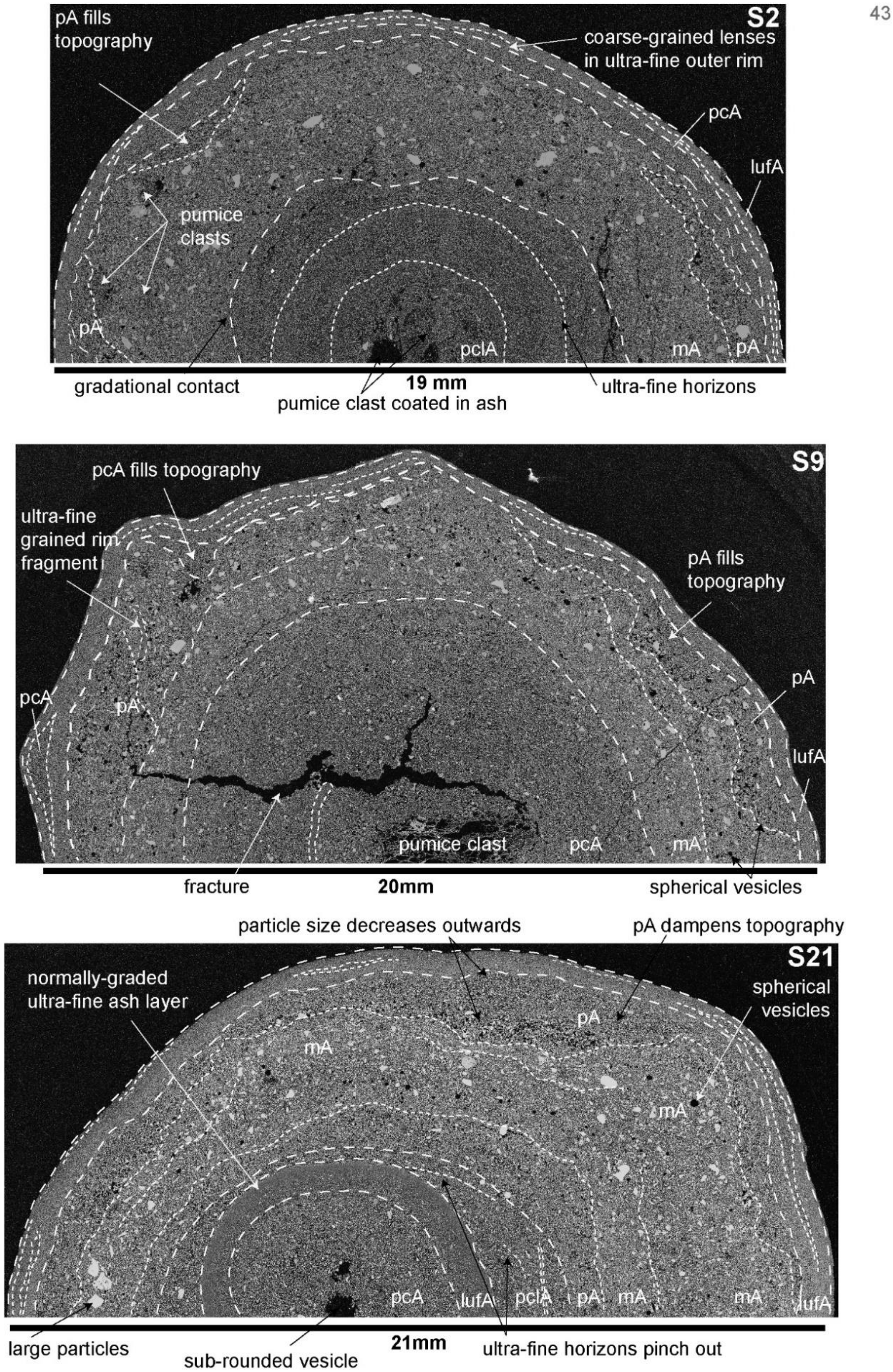

Figure 8. Interpreted backscatter SEM montages of selected accretionary lapilli. Individual facies are distinguishable based on grainsize, porosity, structure, and sorting. Note changing exterior morphology during growth of aggregate. The radial crack in 7b is interpreted as a relic from drying out post-deposition. See Table 1 for facies descriptions.

Layers composed of this facies are typically normally graded and fine outwards (Table 1). This grading is commonly disrupted by discontinuous layers and lenses of slightly coarser ash (Figure 6f). The discontinuous layers thicken slightly into concavities in the underlying layer and act to dampen the irregularities. The lenses have flat bases and convex upper surfaces, are <5 mm long, and are composed of coarser-grained ash <80 μm in diameter (Figure 8 S2, S9). They help define the prominent lumps, 1–4 mm wide, on some aggregates' exteriors (e.g., Figures 3, 6e, 8 S2, S9). The lenses are composed of the porous clustered ash facies (pcA, Figure 6e).

3.2 Internal facies associations and structure

Seven of nine aggregates show a common sequence of facies (Figure 9, Figure 10): (1) a core composed of porous fine ash or porous clustered fine ash (pA/pcA); (2) a concentric layer of massive fine ash (mA); and (3) a second concentric layer of laminated ultrafine ash (lufA). Two aggregates (#10 and #50 in Figure 9) lack outer layers of ultrafine ash.

The core is typically the second most voluminous region within the aggregates (<46% of aggregate radius). Six of the aggregates have cores composed of porous, clustered fine ash (pcA); the cores of the other three are composed of porous ash (pA; Figure 9). The pcA cores of two aggregates contain regions of porous clustered laminated fine ash (pclA); two others contain layers of laminated ultrafine ash (lufA) (Figure 8, S21, S49). In the latter layers, the ash becomes finer grained and better sorted outwards and has a sharp outer contact against the enclosing ash layers (Figure 6b). Millimetre-sized pumice clasts, sub-spherical cavities, or moulds of vegetation occur within the cores of some aggregates (Figure 8).

The cores grade out into a layer of massive fine ash (mA) which forms the thickest layer in most aggregates. This layer can grade both laterally and radially into layers of porous fine ash (pA; e.g. Figure 8, S2, S9). In seven aggregates, discontinuous layers of visibly more porous ash occur within layers of massive fine ash but these layers are quantitatively indistinguishable (Figure 6d). These layers occur within the centre of the mA layer (e.g., Figure 8, S21). Layers of porous ash (pA) occur within six out of nine aggregates exterior to the massive fine ash facies (mA; Figure 9). In these six aggregates there is an undulating contact between the porous fine ash (pA) and the poorly sorted, massive fine ash (mA): this topography strongly influences the aggregates' exterior morphology.

Layers of clustered fine ash (pcA/pclA) are present in five of the nine aggregates as a <1.5 mm thick layer enclosing the porous fine ash facies (pA). When present on the exterior of the massive ash facies (mA), both the porous fine ash facies (pA) and the porous, clustered fine ash facies (pcA) are laterally discontinuous; pinching out between the layers of massive fine ash facies (mA) and laminated, ultrafine ash facies (lufA) or just dissipating laterally (e.g. Figure 8 S2, S9). They thicken into depressions in the outer surface of the massive ash facies (mA), smoothing the outer surface of the aggregate (e.g. Figure 8 S2, S21).

The outermost layer in seven of the aggregates is composed of laminated, ultrafine ash (lufA; Figure 9). These layers are 0.5–0.9 mm thick, but commonly thicken and thin around the perimeter of an ash aggregate, dampening irregularities in subjacent layers (Figure 8). They are typically the thinnest layers in the aggregates (<15% of aggregate radius).

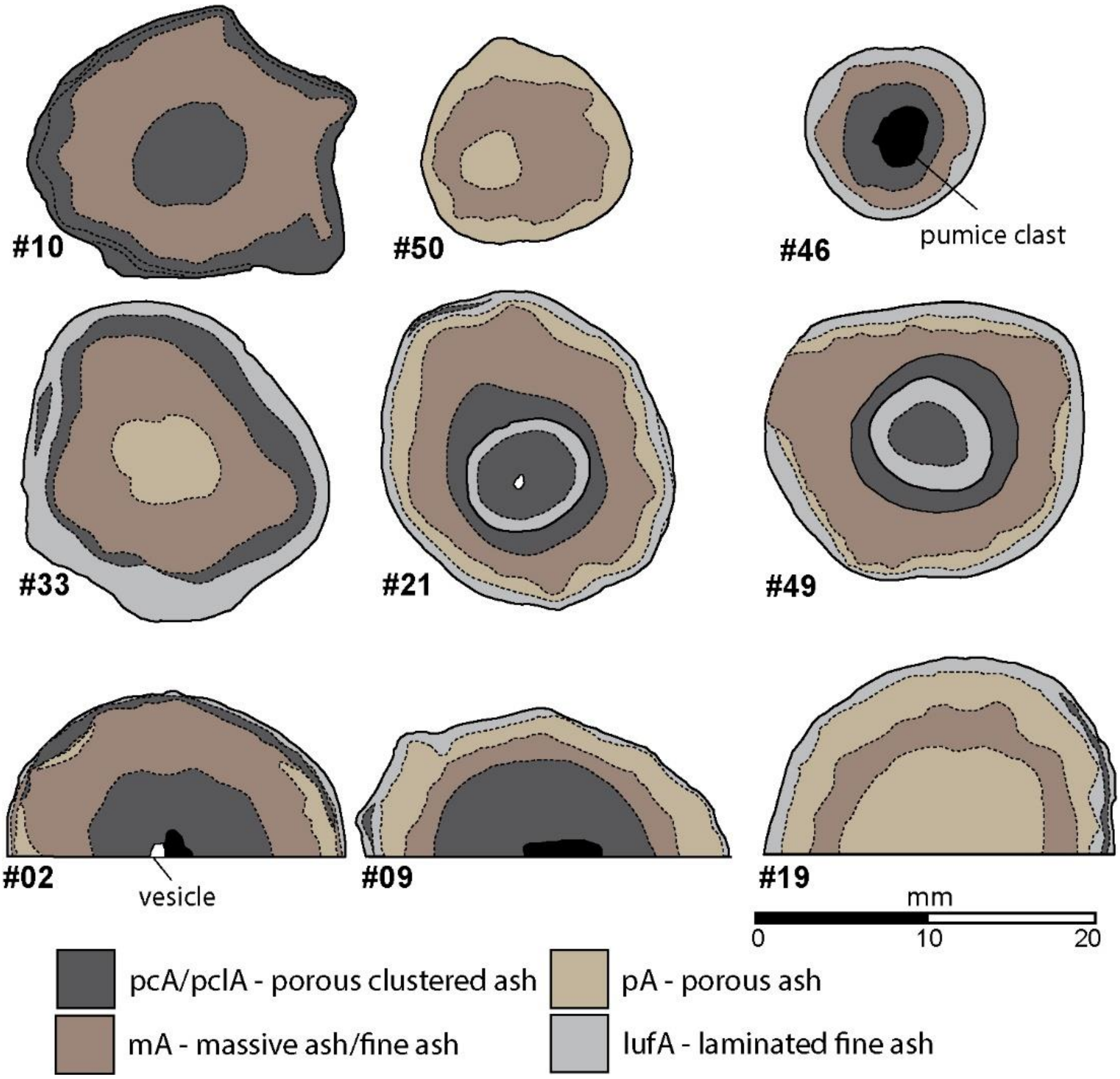

Figure 9. Facies maps for cross-sections through representative accretionary lapilli illustrating the common succession of facies from core outwards. Fine-grained rims are missing from #50 and #10, probably due to abrasion or breakage. See Table 1 for description of facies. Note how the layers of porous ash (pA) and laminated ultrafine ash (lufA) dampen ‘lumps’ within the massive ash (mA) layer; #10 and #33 maintain the shape of these lumps on their exteriors. See Table 1 for facies descriptions.

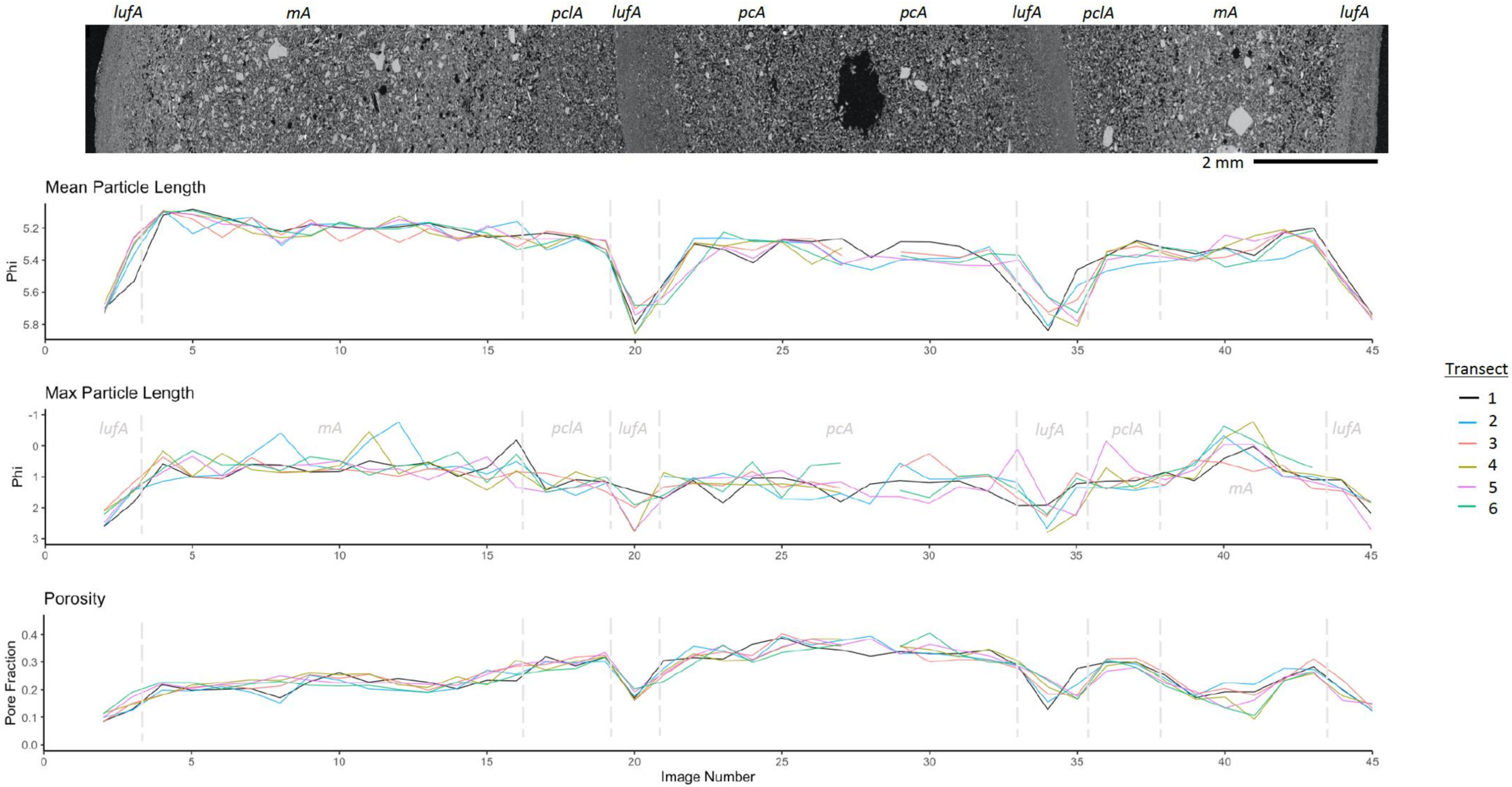

Figure 10. Transects of mean particle length (M_z), maximum particle length and porosity across the centre of sample #21 (see Fig. 7, Fig. 8). Each line corresponds to one transect run across the image from 1 across the top sequentially down to 6. Mean and maximum particle lengths are greatest in the massive, poorly sorted ash facies (mA) and smallest in the ultrafine ash facies (lufA). Porosity is highest in the porous, clustered ash facies (pcA) and least in the ultrafine ash facies (lufA). Maximum particle size is an underestimate for the coarsest facies (mA) as the largest

particles exceeded the field of view. Facies contacts are estimated visually using the SEM image and highlighted on plots by grey dashes. Note that the curved and/or gradational contacts in the image means peaks and troughs on the plots are sometimes staggered as one transect encounters a new facies before the others. Also note the reversed Phi scales for better visualisation. See Table 1 for facies descriptions.

4 Interpretation

The sampled ash aggregates are composed of vitric bubble wall shards and minor volumes of crystals derived from the explosive fragmentation of rhyodacitic magma. Observations of mudstone clasts, clay matrix, diatomite and free diatoms within the aggregates (Figure 7) indicate that lake sediments were incorporated into the eruption column (c.f., Van Eaton et al., 2013). The stratigraphic occurrence of these aggregate types throughout the TBJ's unit D pyroclastic density current deposits (Brown et al., submitted) suggests that they were heavily influenced by the passage of the currents and development of co-ignimbrite ash clouds (c.f., Brown et al, 2010; Van Eaton and Wilson, 2013).

The distinct characteristics of each facies observed in the aggregates, and the presence of multiple texturally distinct layers, indicate that aggregation conditions changed markedly during growth. Variables that may have influenced growth conditions within ash clouds include ambient humidity (ash cloud water content), temperature controlling the abundance of liquid water, vapour or ice in the cloud, ash mass loading and grainsize distribution. Small aggregates such as ash clusters are held together by electrostatic forces and require low humidity conditions to form (e.g. Sorem, 1982; Gilbert et al., 1991; James et al., 2002, 2003). Larger aggregates require hydrostatic bonds to form. Laboratory experiments reveal the availability of liquid water is a dominant control on aggregation (e.g., Gilbert and Lane 1994; Schumacher and Schmincke, 1995; Van Eaton et al., 2012a; Mueller et al., 2016). As liquid water contents increase, so does the maximum range of particle sizes that can be accreted, alongside the maximum size of aggregates formed. This is because of more efficient collisional kinetic energy dispersal and stronger capillary forces at particle contacts (Ennis et al., 1991; Iveson et al., 2001). Liquid water on particle surfaces allows particles to migrate into a more compact framework under pressure (Iveson et al., 2001). Once a critical saturation level is reached (>20–25 wt. % H_2O: Schumacher and Schmincke, 1995; Van Eaton et al., 2012; Mueller et al., 2016), experimental aggregates slurry and are not preserved, indicating an upper humidity limit to ash aggregate formation.

Aggregates may gain strength through the precipitation of salt minerals at particle contacts as they dry, which may occur during fallout. This has been observed in natural ash aggregates (e.g. Gilbert and Lane, 1994; Scolamacchia et al., 2005; Colombier et al., 2019) and experiments (Mueller et al., 2016; Mueller et al., 2017a; Mueller et al., 2017b).

4.1 Porous, clustered fine ash (pcA)

The ash clusters that characterize this facies are similar to those sampled from eruption clouds and co-ignimbrite fallout deposits (e.g., Sorem, 1982; Bonadonna et al., 2002, 2011) and those produced experimentally at very low water contents (<5 wt.%) and held together by electrostatic bonds (Schumacher, 1994; James et al., 2003; Van Eaton et al., 2012a). The ash clusters in this facies form a framework that is texturally similar to that of experimentally-produced clusters (Van Eaton et al. (2012a). These experimental clusters, 100–200 μm in diameter, initially formed under near-dry conditions and then began adhering together as liquid water contents increased. We envisage a similar increase in water contents to account for the formation of the porous, clustered fine ash facies (pcA). The pore space between clusters was preserved because low liquid water contents prevented the particles from rearranging during or after collision with other clusters into a more compact framework (e.g., Iveson et al., 2001). The low water contents (<5 wt. %) may also account for the moderate sorting of this facies: larger particles require stronger capillary forces to stick together after a collision. Particle fabrics are weak because particles accreted as clusters or randomly oriented particles.

We interpret the ultrafine laminations of the clustered, laminated ash sub-facies (pclA) to mark brief periods where agglomeration of clusters transitioned to accretion of individual particles, perhaps during passage through regions of the cloud where water content was too low to form ash clusters.

4.2 Massive fine ash (mA)

The massive, poorly sorted, low porosity nature of this facies, and the presence of spherical vesicles (Figure 6c) closely resembles that of aggregates produced experimentally under wet conditions (~15–25 wt. % liquid water; Schumacher and Schmincke, 1995; Van Eaton et al., 2012a; Mueller et al., 2016). Under such conditions liquid films entirely enveloped particles (Iveson et al., 2001), and particle clusters became water saturated. This allows a wide range of particle sizes to accrete (e.g., Schumacher and Schmincke, 1995; Van Eaton et al., 2012a; Mueller et al., 2016), which accounts for the presence of large particles in this facies. The thicker liquid films more efficiently diffuse collisional kinetic energy and promote successful collisions between larger particles and aggregates (Ennis et al., 1991; Iveson et al., 2001). Capillary forces are also stronger and can retain larger particles post-collision (Schumacher and Schmincke, 1995). In experiments, most ash aggregated within seconds to tens-of-seconds following coating of particles with liquid water (Van Eaton et al. 2012a). Such processes may explain why this facies is the thickest and most voluminous in the TBJ aggregates.

We infer that the low porosity of this facies resulted from thick liquid films that acted as an inter-particle lubricant (Iverson et al., 2001). Accreted particles were able to migrate during mechanical compaction from collisions with other aggregates or particles into a tightly packed particle framework (Blandin et al., 2003; Pitt et al., 2018). The spherical vesicles appear similar to those in vesiculated tuffs (e.g. Lorenz, 1974; Rosi, 1992) and lahar deposits (e.g., Pierson, 1985; Major and Voight, 1986), as well as those in both natural aggregates (Lorenz, 1974) and aggregates formed in experiments under saturated conditions (Van Eaton et al., 2012a). High aggregation rates resulting from high liquid water contents (e.g. Van Eaton et al., 2012a; Mueller et al., 2016) could have trapped pore space, which then coalesced during agitation and mechanical compaction to form spherical vesicles (Lorenz, 1974; Major and Voight, 1986; Rosi, 1992; Capaccioni and Coniglio, 1995; Van Eaton et al., 2012a). Vesicle growth could have been accommodated by elastic deformation of the surrounding liquid-particle mixture (Sills et al., 1991; Boudreau et al., 2005).

The mm-scale lumps on the exterior of layers of this facies (Figures 3 and 8) are interpreted as the result of the collision of smaller water-saturated aggregates (ash pellets, or AP1 aggregates of Brown et al., 2012), as observed in experiments under saturated conditions (~10–22 wt.% liquid water Van Eaton et al., 2012a; >25 w.t.% Schumacher and Schmincke 1995). These lumps have been seen on large ash aggregates at other volcanoes (Schumacher and Schmincke 1995; Van Eaton et al., 2012a). We infer that the colliding aggregates deformed on impact due to inter-particle lubrication and accreted due to efficient kinetic energy dispersal and strong capillary forces at particle contacts. The entire layer may have been accreted via this process. Rapid aggregation of material under saturated conditions would have increased the aggregate's terminal velocity, promoting further collisions (c.f., hailstone formation, Pflaum, 1980; Iveson, 2001).

We infer that the porous fine ash (pA) sub-facies formed under a saturation condition that was insufficient for particles to rearrange and compact, but high enough to prevent clustering (~10 wt.% liquid water by analogy with experiments of Van Eaton et al. 2012). The less irregular outer surface of layers of porous fine ash may have resulted from the accretion of smaller aggregates and individual particles: the weak particle fabric may indicate that particles accreted individually, rather than as colliding aggregates.

4.3 Laminated ultrafine ash (lufA)

The fine grainsize, fining-outwards trend, and multiple thin laminations characteristic of this facies (Figure 6e, f and Figure 8) indicates that the aggregates experienced a marked change in aggregation conditions. The presence of this facies as the outer layer of most aggregates indicates that the region(s) in which this facies was accreted was close in either time or space, or both, to their deposition from pyroclastic density currents.

The conditions under which this facies accreted remain unclear. Similar fine-grained, laminated outer rims in other aggregates have been interpreted as the result of a gradual decrease in liquid water availability during aggregate descent into warmer, lower portions of the co-ignimbrite plumes and ground-hugging currents (Schumacher and Schmincke, 1995; Brown et al., 2010; Van Eaton et al., 2012a).

Mueller et al. (2016) proposed that ultrafine rim growth is dependent upon the relative size of colliding bodies: once an aggregate exceeds a certain size, collisional kinetic energy dispersal is insufficient for particles >60 um, particle clusters, or other aggregates to accrete. The presence of lenses of clustered fine ash in the laminated ultra-fine facies (Figure 6e and Figure 8), most simply interpreted as larger aggregates that collided and deformed like the mm-scale lumps in the massive ash (mA) facies, seems counter to a collisional energy control on accreted particle size.

We infer that this facies (lufA) formed when the TBJ aggregates encountered a dilute plume region with a predominantly ultrafine grainsize distribution and low liquid water contents (<5 wt.% liquid water following Van Eaton et al., 2012b). The low (<5 wt.%) water contents were insufficient to efficiently disperse collisional kinetic energy and capillary forces could not bind particles >60 μm in diameter. Thus only fine ash <60 μm in diameter could accrete. The tightly-packed structure of the laminated ultrafine ash facies (lufA), mirrored in the rims of Van Eaton et al. (2012a)'s experimental aggregates, suggests aggregates grew within an ash cloud composed of particles predominantly <10 μm in diameter. Coarser-grained laminations within the ultrafine rims (Figure 6f) may indicate brief increases in water availability that allowed a wider range of particle sizes to successfully accrete.

5 Discussion

5.1 Comparison with other aggregates.

The TBJ aggregates are similar in size, shape, density and terminal fall velocities to large, complex aggregates produced during other ignimbrite-forming, water-rich eruptions (e.g. Van Eaton and Wilson, 2013; Burns et al., 2017; Figure 5). Rim-type accretionary lapilli from Laacher See volcano, Germany, contain coarse-grained cores surrounded by fine-grained, commonly laminated rims that fine outwards (Schumacher and Schmincke, 1991). Accretionary lapilli in ignimbrites on Tenerife are also subspherical, <25 mm in diameter and contain coarse cores surrounded by finer-grained, concentric laminations that thicken and thin according to the underlying topography (Brown and Branney, 2004; Brown et al., 2010). Layered aggregates from the 25.4 ka Oruanui eruption, New Zealand, are <30 mm in diameter with particles concentrically orientated in the outer layers and complexly layered aggregates exhibit massive, vesicular inner regions surrounded by finely laminated outer layers (Van Eaton and Wilson, 2013). These similarities indicate that the TBJ aggregates provide a reasonable template for understanding the formation and growth of large, complex aggregates in a range of ignimbrite-forming eruptions. One notable feature of the TBJ aggregate population is the somewhat thin outermost layer of ultrafine ash (<1 mm thick), which is comparable to the layered or complexly layered accretionary lapilli described of the Oruanui eruption (Van Eaton and Wilson, 2013, their table 1). The complexly layered Oruanui aggregates are distinct from the ultrafine rim-type types, which have thicker rims (1–2 mm). The implication is that the multiple-laminated examples with thinner rims may represent an end-member version of growth during passage through rapidly changing, stratified regions of co-ignimbrite plumes and ground-hugging currents.

5.2 Aggregate growth pathways

The sequential occurrence of the three main facies indicates that the majority of the sampled aggregates followed a broadly similar growth path: a porous, clustered fine ash (pcA) core is enclosed by massive fine ash facies (mA), which is enclosed by ultrafine ash facies (lufA) (Figure 9). The repetition of certain facies within this order (e.g. pcA cores and also pcA regions beneath the ultrafine rim, e.g. Figure 9, S2) indicates the conditions favourable to these layers' formation was encountered multiple times during the aggregate's growth. Aggregates with a poorly sorted fine ash core (pA or mA: Figure 9 #19, #33, #50) are interpreted either as aggregates whose formation initiated at a later stage along this path, or whose clustered interior structure was removed via subsequent saturation. Saturation could either occur due to the infiltration of water following collision with other saturated aggregates or water droplets, or due to the melting of a hailstone core. The aggregates that contain a layer of lufA close to their cores (#21 and #49 in Figure 9) may have undergone recycling within the ash cloud, perhaps by being caught in strong updrafts.

The growth process inferred here for the formation of the porous, clustered fine ash facies (pcA) and the massive fine ash facies (mA), whereby aggregation occurs by the accretion of multiple smaller aggregates, rather than by the accretion of individual particles (e.g., Iveson et al., 2001; James et al., 2003; Van Eaton et al., 2012a), could explain the observed rapid formation (minutes to tens of minutes) of natural ash aggregates (e.g., Gilbert and Lane, 1994). In this manner aggregates accumulate significant amounts of material from one collision, rather than assembling particle-by-particle. Additional evidence for the accretion of smaller aggregates onto larger ones is given by the irregular, lumpy relief of the massive fine ash layer (Figure 8, Figure 9), and by the lenses of coarser-grained material within the outer layers of laminated ultrafine ash (Figure 6e).

Fragmented ultrafine rims within the host PDC deposit (Brown et al., submitted) indicate disaggregation was also an active process. Experimental and natural disaggregation due to in-flight collisions or landing is well documented (James et al., 2002; Taddeucci et al., 2011; Van Eaton et al., 2012a; Van Eaton and Wilson, 2013; Mueller et al., 2017b). Calculated fall velocities for TBJ aggregates exceed experimental disaggregation impact velocities for non-structured aggregates (Mueller et al., 2017b) and are likely underestimates due to proximal falling particles or aggregates disturbing the local airflow (Del Bello et al., 2017). Without visible evidence of mineral precipitation at particle contacts, how the internal features of preserved complex TBJ aggregates withstood any disaggregation processes remains unclear.

5.3 Conceptual model

We develop a conceptual model to explain the growth of the TBJ aggregates based on aggregation processes occurring predominantly within co-ignimbrite plumes (Figure 11). We envisage that during the eruption multiple co-ignimbrite plumes rose from the pyroclastic density currents over substantial areas around the caldera. These plumes interacted with the vent-derived ash clouds to produce hybrid clouds with multiple spreading levels, similar to that proposed for the 25.4 ka Orunaui eruption, New Zealand (Van Eaton et al., 2012b; Houghton et al., 2015).

Ash clusters represent the first stage of aggregation. During the emplacement of unit D pyroclastic density currents, conditions suitable for the growth of ash clusters (very low or absent liquid water contents) would have occurred at the lateral edges of the lower plume or where liquid water was supercooled at high altitudes (>10 km) and so froze on contact with particles (Van Eaton et al., 2015) (Figure 11). In these conditions liquid water was scarce (<5 wt. %, Van Eaton et al., 2012a) and ash particles stuck together through weak electrostatic forces and small amounts of liquid water. This resulted in the growth of loose particle clusters. Descent of these loosely bound clusters to warmer, lower altitudes or entrainment in eddies into warmer inner regions of the plume resulted in greater abundances of water being available to the clusters. We infer melting of ice coatings and contact with increasingly abundant condensed liquid water droplets increased saturation levels in the clusters. Collisions at this stage resulted in larger aggregates (ash pellets) formed from multiple accreted ash clusters (facies pcA) (Figure 11A).

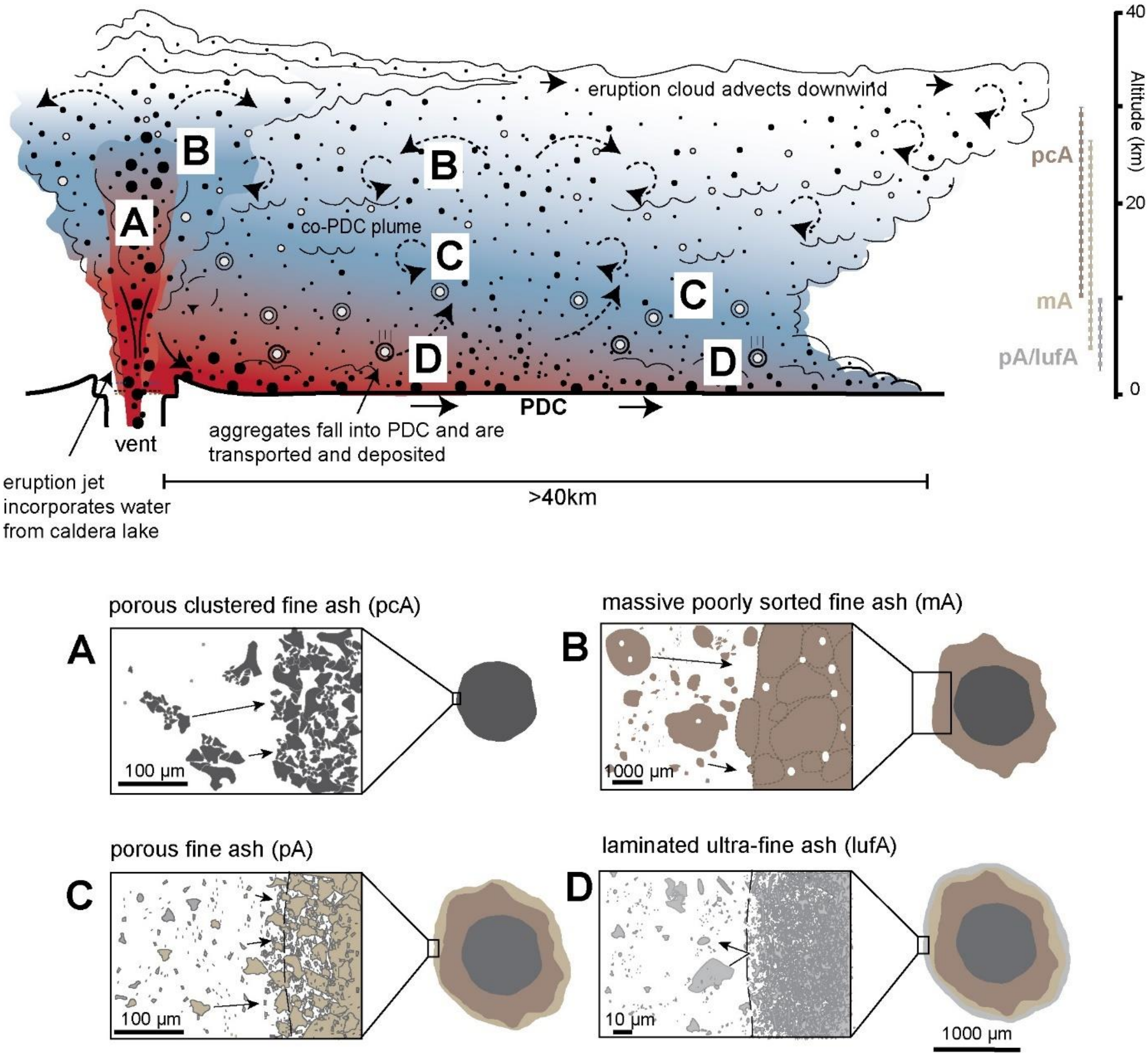

Figure 11. Conceptual model for the formation of complex ash aggregates during the emplacement of unit D of the Tierra Blanca Joven eruption. Aggregation occurs within vent-derived plumes and co-PDC plumes lofted from pyroclastic density currents. Letters A–D give the inferred locations and processes involved in formation of key aggregate facies. Color shading gives a qualitative indication of warmer regions of the clouds (red) and cooler regions where liquid water and/or ice would be present (blue to white). Altitude scale is approximate. In top diagram, black dots indicate pumice fragments and white dots indicate ash aggregates. See Table 1 for facies terms.

Descent into warmer altitudes and/or re-entrainment towards the wet regions of the plume increased the abundance of liquid water, resulting in saturated aggregation conditions and the formation of the massive fine ash facies (mA). The efficient dispersal of collisional kinetic energy by thick liquid films (Iveson et al., 2001), and strong capillary forces from liquid bridges (Schumacher and Schmincke, 1995) allowed a wider range of particle sizes to accrete (Van Eaton et al., 2012a). Aggregates subjected to these conditions predominantly grew by the accretion of smaller, saturated aggregates <4 mm diameter (Figure 11B). The high efficiency of accretion under saturated conditions (e.g., Schumacher and Schmincke, 1995) resulted in rapid growth which increased terminal fall velocities and promoted further collisions with ash particles, aggregates or water droplets (e.g., Gilbert and Lane, 1994; Iveson et al., 2001).

Rapid growth continued until the aggregates were not supported by updrafts within co-ignimbrite plumes. During descent they encountered increasingly warmer and drier conditions in the lower parts of co-ignimbrite plumes or upper parts of stratified pyroclastic density currents (Figure 11), which were composed of primarily ultrafine ash (<63 μm, enriched in <10 μm; see Brown et al., 2010; Van Eaton and Wilson, 2013). These conditions were conducive to particle-by-particle accretion of the ultrafine rims (facies lufA) primarily by weak hydrostatic forces within the dilute cloud. Fining outwards suggests a gradual decrease in the strength of hydrostatic binding forces and aggregate saturation, possibly due to rising temperatures at progressively lower levels in the co-ignimbrite/pyroclastic density current system. Aggregates with interior layers of laminated, ultrafine facies (lufA) probably resulted from re-entrainment into the hotter, drier region of the ash cloud-pyroclastic density current system without being entrained towards wet regions of the plume (which would have accreted larger particles). Subsequent re-entrainment returned them to the regions conducive to pcA formation and accretion (Figure 11). After they had fallen into the lower regions of pyroclastic density currents the aggregates were deposited alongside ash and pumice lapilli.

6 Conclusions

High resolution SEM imaging has facilitated quantitative analysis of a population of complex accretionary lapilli from pyroclastic density current deposits of the Phreatoplinian Tierra Blanca Joven (TBJ) eruption, Ilopango Caldera, El Salvador. We describe three principal facies that differ in terms of particle size distribution, porosity, and particle alignment. Each facies resulted from ambient conditions that differed in the availability of liquid water, particle concentration and maximum particle size at different regions within the ash clouds. The characteristic sequence of facies indicates that most aggregates shared a common growth history during fallout from ash clouds. Aggregation of fine ash particles initiated in sub-saturated conditions at the edges of a vent-derived or co-ignimbrite plume to form loose particle clusters, ~20–60 μm in diameter. These ash clusters collided with each other and formed subspherical ash pellets. After descending to warmer, wetter levels of the plume they accreted a poorly sorted, massive layer of ash comprising the bulk of each aggregate. Finally, they descended through a co-ignimbrite cloud rich in ultrafine ash before being deposited out of the base of the pyroclastic density current. The bulk of the aggregates was constructed via accretion of smaller aggregates (clusters and pellets) rather than by individual particle-by-particle accretion. Our results indicate a growth pathway for the ash aggregates studied here, and perhaps more broadly for complex accretionary lapilli observed in a range of different eruption deposits, involving systematic changes in layer characteristics defined by porosity, grainsize, and particle alignment.

Acknowledgements

This research was part-funded by National Geographic Committee for Research and Exploration grant awarded to Brown (grant number GEFNE7-11). Van Eaton acknowledges NSF Postdoctoral Fellowship EAR1250029. We are grateful to Bruce Houghton and Jim Vallance for introducing us to the TBJ and for assistance during fieldwork. We thank the Ministerio de Ambiente y Recursos Naturales, El Salvador, for logistical support, and Alex Chavez, Cecilia Polio, Demetrio Escobar, and Carlos Pullinger for field assistance. We thank Leon Bowen for invaluable assistance and expertise during collection of data on the SEM. We thank Mike Branney and Claire Horwell for comments on the Master's thesis from which this study originated. We thank Jim Vallance, Larry Mastin, Ulrich Kueppers and an anonymous reviewer for insightful reviews of the manuscript. Any use of trade, firm, or product names is for descriptive purposes only and does not imply endorsement by the U.S. Government.

CRediT author statement

Henry Hoult: investigation, writing – original draft, review and editing. **Richard Brown:** conceptualization, funding acquisition, project administration, investigation, writing – review and editing. **Alexa R Van Eaton:** conceptualization, investigation, writing - review and editing **Walter Hernandez**: project administration, investigation, writing - review and editing. **Kate Dobson:** investigation, writing - review and editing. **Bryan Woodward:** investigation.

Declaration of competing interest

The authors declare that they have no known competing financial interests or personal relationships that could have appeared to influence the work reported in this paper.

References

Blandin, A.F., Mangin, D., Rivoire, A., Klein, J.P. and Bossoutrot, J.M., 2003. Agglomeration in suspension of salicylic acid fine particles: influence of some process parameters on kinetics and agglomerate final size. Powder Technol., 130(1–3): 316–323.

Bonadonna, C., Mayberry, G.C., Calder, E.S., Sparks, R.S.J., Choux, C., Jackson, P., Lejeune, A.M., Loughlin, S.C., Norton, G.E., Rose, W.I., Ryan, G. and Young, S.R., 2002. Tephra fallout in the eruption of Soufriere Hills Volcano, Montserrat. Geol. Soc. Lond. Mem. 21(1): 483-516.

Bonadonna, C., Genco, R., Gouhier, M., Pistolesi, M., Cioni, R., Alfano, F., Hoskuldsson, A. and Ripepe, M., 2011. Tephra sedimentation during the 2010 Eyjafjallajökull eruption (Iceland) from deposit, radar, and satellite observations. J. Geophys. Res., 116: B12202, https://doi:10.1029/2011JB008462

Boudreau, B., Algar, C., Johnson, B.D., Croudace, I., Reed, A., Furukawa, Y., Dorgan, K.M., Jumars, P.A., Grader, A.S., Gardiner, B.S.; Bubble growth and rise in soft sediments. Geol. 2005;; 33: 517–520. https://doi.org/10.1130/G21259.1

Branney, M.J., Bonnichsen, B., Andrews, G.D.M., Ellis, B., Barry, T.L. and McCurry, M., 2008. 'Snake River (SR)-type'volcanism at the Yellowstone hotspot track: distinctive products from unusual, high-temperature silicic super-eruptions. Bull. Volcanol. 70: 293-314. https://doi.org/10.1007/s00445-007-0140-7

Brown, R.J. and Branney, M.J., 2004. Event-stratigraphy of a caldera-forming ignimbrite eruption on Tenerife: the 273 ka Poris Formation. Bulletin of Volcanology. 66(5):392-416. https://doi.org/10.1007/s00445-003-0321-y

Brown, R.J., Branney, M.J., Maher, C. and Harris, P.D., 2010. Origin of accretionary lapilli within ground-hugging density currents: Evidence from pyroclastic couplets on Tenerife. Geol. Soc. Am. Bull., 122: 305-320. https://doi.org/10.1130/B26449.1

Brown, R.J., Bonadonna, C. and Durant, A.J., 2012. A review of volcanic ash aggregation. Phys. Chem. Earth. 45–46: 65–78, https://doi.org/10.1016/j.pce.2011.11.001

Brown, R.J., Van Eaton, A.R., Hernandez, W., Tournigand, P.-Y., Sweeney, C. and Vallance, J.W., Submitted. Ash aggregate-rich pyroclastic density currents of the 431 CE Tierra Blanca Joven eruption, Ilopango Caldera, El Salvador. J. Volcanol. Geotherm. Res.

Burns, F.A., Bonadonna, C., Pioli, L., Cole, P.D. and Stinton, A., 2017. Ash aggregation during the 11 February 2010 partial dome collapse of the Soufrière Hills Volcano, Montserrat. J. Volcanol. Geotherm. Res., 335: 92-112, https://doi.org/10.1016/j.jvolgeores.2017.01.024

Capaccioni, B. and Coniglio, S., 1995. Varicolored and vesiculated tufts from La Fossa volcano, Vulcano Island (Aeolian Archipelago, Italy): evidence of syndepositional alteration processes. Bull. Volcanol., 57: 61–70, https://doi.org/10.1007/BF00298708

Carey, S.N. and Sigurdsson, H., 1982. Influence of particle aggregation on deposition of distal tephra from the MAy 18, 1980, eruption of Mount St. Helens volcano. J. Geophys. Res., 87(B8): 7061–7072, https://doi.org/10.1029/JB087iB08p07061

Colombier, M., Mueller, S.B., Kueppers, U., Scheu, B., Delmelle, P., Cimarelli, C., Cronin, S.J., Brown, R.J., Tost, M., Dingwell, D.B., 2019. Diversity of soluble salt concentrations on volcanic ash aggregates from a variety of eruption types and deposits. Bull. Volcanol., 81(7): 39, 1-13. https://doi.org/10.1007/s00445-019-1302-0

Del Bello, E., Taddeucci, J., Scarlato, P., Andronico, D., Scollo, S., Kueppers, U. and Ricci, T., 2017. Effect of particle volume fraction on the settling velocity of volcanic ash particles: insights from joint experimental and numerical simulations. Sci. Reports, 7(1):1-11. https://doi.org/10.1038/srep39620

DeMets, C., Gordon, R.G. and Argus, D.F., 2010, Geologically current plate motions. Geophys. J. Int. 181: 1-80 https://doi.org/10.1111/j.1365-246X.2009.04491.x

Dull, R.A., Southon, J.R. and Sheets, P., 2001. Volcanism, ecology and culture: A reassessment of the Volcán Ilopango Tbj eruption in the Southern Maya realm. Lat. Am. Antiq., 12(1): 25–44, https://doi.org/10.2307/971755

Dull, R.A., Southon, J.R., Kutterolf, S., Anchukaitis, K.J., Freundt, A., Wahl, D.B., Sheets, P., Amaroli, P., Hernandez, W., Wiemann, M.C. and Oppenheimer, C., 2019. Radiocarbon and geologic evidence reveal Ilopango volcano as source of the colossal ‘mystery’ eruption of 539/40 CE. Quat. Sci. Rev., 222: 105855, https://doi.org/10.1016/j.quascirev.2019.07.037

Durant, A.J. and Rose, W.I., 2009. Sedimentological constraints on hydrometeor-enhanced particle deposition: 1992 eruptions of Crater Peak, Alaska. J. Volcanol. Geotherm. Res., 186: 40-59, https://doi.org/10.1016/j.jvolgeores.2009.02.004

Durant, A.J., Brown, R.J. (2016). Ash aggregation in volcanic clouds. In: Mackie, S., Cashman, K., Ricketts, H, Rust A., Watson, M., (Eds) Volcanic Ash: Hazard observation, Elsevier, pp. 53-65.

Ennis, B.J., Tardos, G. and Pfeffer, R., 1991. A microlevel-based characterization of granulation phenomena. Powder Tech., 65(1-3): 257-272. https://doi.org/10.1016/0032-5910(91)80189-P

Folk, R.L. and Ward, W.C., 1957. Brazos River bar: a study in the significance of grain size parameters. J. Sediment. Petrol., 27(1): 3-26, https://doi.org/10.1306/74D70646-2B21-11D7-8648000102C1865D

Gilbert, J.S., Lane, S., Sparks, R. and Koyaguchi, T., 1991. Charge measurements on particle fallout from a volcanic plume. Nature, 349: 598-600, https://doi.org/10.1038/349598a0

Gilbert, J.S. and Lane, S.J., 1994. The origin of accretionary lapilli. Bull. Volcanol., 56: 398-411, https://doi.org/10.1007/BF00326465

Hart, W.J.E. and Steen-McIntyre, V, 1983. Tierra Blanca Joven tephra from the AD260 Eruption of Ilopango Caldera. In: Sheets, P.D., (Ed) Archaeology and Volcanism in Central America: The Zapotitán Valley of El Salvador, pp. 15-34.

Houghton, B.F., White, J.D., Van Eaton, A.R. (2015). Phreatomagmatic and related eruption styles. In: H. Sigurdsson, B.F. Houghton, H. Rymer, J. Stix and S.R. McNutt (Editors), The Encyclopedia of Volcanoes. Academic Press, San Diego, California, pp. 537-552.

Iveson, S.M., Litster, J.D., Hapgood, K. and Ennis, B.J., 2001. Nucleation, growth and breakage phenomena in agitated wet granulation processes: a review. Powder Technol., 117(1-2): 3-39, https://doi.org/10.1016/S0032-5910(01)00313-8

James, M.R., Gilbert, J.S. and Lane, S.J., 2002. Experimental investigation of volcanic particle aggregation in the absence of a liquid phase, J. Geophys. Res., 107: 2191, https://doi.org/10.1029/2001JB000950

James, M.R., Lane, S.J. and Gilbert, J.S., 2003. Density, construction, and drag coefficient of electrostatic volcanic ash aggregates, J. Geophys. Res., 108: 2435, https://doi.org/10.1029/2002JB002011

Kutterolf, S., Freundt, A. and Peréz, W., 2008. Pacific offshore record of plinian arc volcanism in Central America: 2. Tephra volumes and erupted masses. Geochem. Geophys. Geosyst., 9(2): Q02S02, https://doi.org/10.1029/2007GC001791

Lorenz, V., 1974. Vesiculated tuffs and associated features. Sed., 21: 273-291, https://doi.org/10.1111/j.1365-3091.1974.tb02059.x

Major, J.J. and Voight, B., 1986. Sedimentology and clast orientations of the 18 May 1980 southwest-flank lahars, Mount St. Helens, Washington. J. Sed. Res., 56: 691-705, https://doi.org/10.1306/212F8A1C-2B24-11D7-8648000102C1865D

Mann, C.P., Stix, J., Vallance, J.W. and Richer, M., 2004. Subaqueous intracaldera volcanism, Ilopango Caldera, El Salvador, Central America. Spec. Papers. Geol. Soc. Am., 2004: 159-174.

Mueller, S.B., Kueppers, U., Ayris, P.M., Jacob, M. and Dingwell, D.B., 2016. Experimental volcanic ash aggregation: Internal structuring of accretionary lapilli and the role of liquid bonding. Earth Planet. Sci. Lett., 433: 232-240, https://doi.org/10.1016/j.epsl.2015.11.007

Mueller, S.B., Ayris, P.M., Wadsworth, F.B., Kueppers, U., Casas, A.S., Delmelle, P., Taddeucci, J., Jacob, M. and Dingwell, D.B., 2017a. Ash aggregation enhanced by deposition and redistribution of salt on the surface of volcanic ash in eruption plumes. Sci. Reports, 7(1):1-9, https://doi.org/10.1038/srep45762

Mueller, S.B., Kueppers, U., Ametsbichler, J., Cimarelli, C., Merrison, J.P., Poret, M., Wadsworth, F.B. and Dingwell, D.B., 2017b. Stability of volcanic ash aggregates and break-up processes. Sci. Reports, 7(1):1-11, https://doi.org/10.1038/s41598-017-07927-w

Pedrazzi, D., Sunye-Puchol, I., Aguirre-Díaz, G., Costa, A., Smith, V.C., Poret, M., Dávila-Harris, P., Miggins, D.P., Hernández, W. and Gutiérrez, E., 2019. The Ilopango Tierra Blanca Joven (TBJ) eruption, El Salvador: Volcano-stratigraphy and physical characterization of the major Holocene event of Central America. J. Volcanol. Geotherm. Res., 377: 81-10, https://doi.org/10.1016/j.jvolgeores.2019.03.006

Pierson, T.C., 1985. Initiation and flow behavior of the 1980 Pine Creek and Muddy river lahars, Mount St. Helens, Washington. Geol. Soc. America Bull., 96: 1056-1069, https://doi.org/10.1130/0016-7606(1985)96<1056:IAFBOT>2.0.CO;2

Pflaum, J.C., 1980. Hail formation via microphysical recycling. J. Atmos. Sci., 37(1): 160-173, https://doi.org/10.1175/1520-0469(1980)037<0160:HFVMR>2.0.CO;2

Pitt, K., Peña, R., Tew, J.D., Pal, K., Smith, R., Nagy, Z.K. and Litster, J.D., 2018. Particle design via spherical agglomeration: A critical review of controlling parameters, rate processes and modelling. Powder Technol., 326: 327-343, https://doi.org/10.1016/j.powtec.2017.11.052

Rosi, M., 1992. A model for the formation of vesiculated tuff by the coalescence of accretionary lapilli. Bull. Volc., 54: 429-434, https://doi.org/10.1007/BF00312323

Scolamacchia. T., Macías, J.L., Sheridan, M.F. and Hughes, S.R., 2005. Morphology of ash aggregates from wet pyroclastic surges of the 1982 eruption of El Chichón Volcano, Mexico. Bull. Volcanol., 68:171-200, https://doi.org/10.1007/s00445-005-0430-x

Schumacher, R. and Schmincke, H.U., 1991. Internal structure and occurrence of accretionary lapilli—a case study at Laacher See Volcano. Bull. Volcanol., 53:612-634, https://doi.org/10.1007/BF00493689

Schumacher, R., 1994. A reappraisal of Mount St. Helens' ash clusters-depositional model from experimental observation. J. Volcanol. Geotherm. Res. 59: 253-260 https://doi.org/10.1016/0377-0273(94)90099-X

Schumacher, R. and Schmincke, H.U., 1995. Models for the origin of accretionary lapilli. Bull. Volcanol. 56: 626-639, https://doi.org/10.1007/BF00301467

Sills, G.C., Wheeler, S.J., Thomas, S.D. and Gardner, T.N., 1991. Behaviour of offshore soils containing gas bubbles. Geotechnique. 41:227-241. https://doi.org/10.1680/geot.1991.41.2.227

Smith, V.C., Costa, A., Aguirre-Diaz, G., Pedrazzi, D., Scifo, A., Plunkett, G., Poret, M., Tournigand, P.Y., Miles, D., Dee, M.W., McConnell, J.R., Sunye-Puchol, I., Harris, P.D., Sigl, M., Pilcher, J.R., Chellman, N. and Gutierrez, E., 2020. The magnitude and impact of the 431 CE Tierra Blanca Joven eruption of Ilopango, El Salvador. Proc. Natl. Acad. Sci., 117(42): 26061-26068, https://doi.org/10.1073/pnas.2003008117

Sorem, R.K., 1982. Volcanic ash clusters: tephra rafts and scavengers. J. Volcanol. Geotherm. Res., 13(1-2): 63-71, https://doi.org/10.1016/0377-0273(82)90019-1

Taddeucci, J., Scarlato, P., Montanaro, C., Cimarelli, C., Del Bello, E., Freda, C., Andronico, D., Gudmundsson, M.T. and Dingwell, D.B., 2011. Aggregation-dominated ash settling from the Eyjafjallajökull volcanic cloud illuminated by field and laboratory high-speed imaging. Geology, 39: 891-894, https://doi.org/10.1130/G32016.1

Telling, J., Dufek, J. and Shaikh, A., 2013. Ash aggregation in explosive volcanic eruptions. Geophys. Res. Lett. 40(10): 2355-2360, https://doi.org/10.1002/grl.50376

Textor, C., Graf, H.-F., Herzog, M., Oberhuber, J.M., Rose, W.I. and Ernst, G.G.J., 2006. Volcanic particle aggregation in explosive eruption columns. Part I: Parameterization of the microphysics of hydrometeors and ash. J. Volcanol. Geotherm. Res., 150: 359-377, https://doi.org/10.1016/j.jvolgeores.2005.09.007

Van Eaton, A.R., Muirhead, J.D., Wilson, C.J.N. and Cimarelli, C., 2012a. Growth of volcanic ash aggregates in the presence of liquid water and ice: an experimental approach. Bull. Volcanol., 74(9): 1963–1984, https://doi.org/10.1007/s00445-012-0634-9

Van Eaton, A.R., Herzog, M., Wilson, C.J.N. and McGregor, J., 2012b. Ascent dynamics of large phreatomagmatic eruption clouds: The role of microphysics. J. Geophys. Res., 117: B03203, https://doi.org/10.1029/2011JB008892

Van Eaton, A.R. and Wilson, C.J.N., 2013. The nature, origins and distribution of ash aggregates in a large-scale wet eruption deposit: Oruanui, New Zealand. J. Volcanol. Geotherm. Res., 250: 129-154, https://doi.org/10.1016/j.jvolgeores.2012.10.016

Van Eaton, A.R., Harper, M.A. and Wilson, C.J.N., 2013. High-flying diatoms: Widespread dispersal of microorganisms in an explosive volcanic eruption. Geology, 41(11): 1187–1190, https://doi.org/10.1130/G34829.1

Van Eaton, A.R., Mastin, L.G., Herzog, M., Schwaiger, H.F., Schneider, D.J., Wallace, K.L. and Clarke, A.B., 2015. Hail formation triggers rapid ash aggregation in volcanic plumes. Nat. Commun., 6: 7860, https://doi.org/10.1038/ncomms8860

Wallace, K.L., Schaefer, J.R. and Coombs, M.L., 2013. Character, mass, distribution, and origin of tephra-fall deposits from the 2009 eruption of Redoubt Volcano, Alaska—highlighting the significance of particle aggregation. J. Volcanol. Geotherm. Res., 259: 145-169, https://doi.org/10.1016/j.jvolgeores.2012.09.015

Zingg, T., 1935. Beitrag zur schotteranalyse. Schweitz. Mineral. Petrogr. Mitt., https://doi.org/10.3929/ethz-a-000103455

Type Image	***Description***	***Occurrence***	***Boundaries***	***Sub-facies***
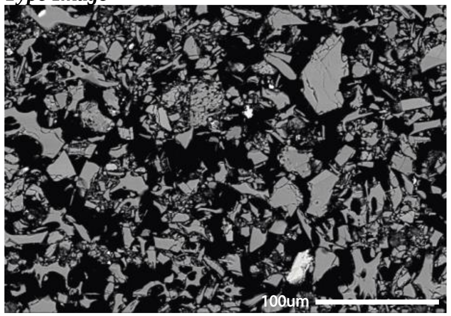	Porous, clustered fine ash [**pcA**] Moderately sorted fine ash with a massive structure composed of ash clusters ~20-60 µm in diameter; particles visually lack preferential orientation; rare large clasts <500 µm; porosity is ~30%; typical thickness ~2.8 mm; max. particle length ~1.12 mm; M_z ~23 µm; σ_i ~1 phi; forms <46% of aggregate radius.	Commonly forms interior of aggregates; can occur in thin truncated lamina or lenses exterior to mA that infill topography and abruptly grade outward into luf*A*.	*Inner*: Gradational from *mA/pA* when not forming the aggregate's core. *Outer:* Gradational and sub-spherical; when forming the aggregate's interior region, it coarsens outwards into *mA*; when forming lenses or lamina towards the outer rim, it fines into lufA.	Porous, clustered, laminated fine ash [**pclA**] As *pcA* but exhibits lamina indicated by fines-rich horizons <100 µm thick, usually laterally non-continuous; particles commonly aligned parallel to lamina.
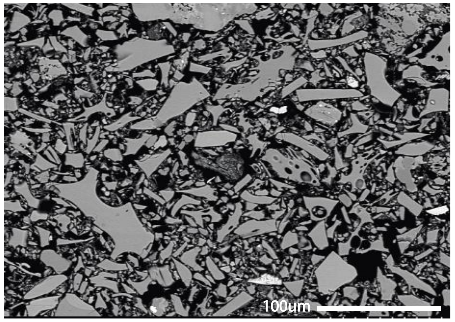	Massive fine ash [**mA**] Very poorly sorted fine ash with a low porosity, massive framework; contains particles <2 mm and sub-rounded vesicles <150 µm; particles visually lack preferential orientation; porosity is ~20%; typical facies thickness ~4.5 mm; max. particle length ~1.83 mm; M_z ~26 µm; σ_i ~1 phi; forms <90% of aggregate radius.	Occurs midway between the core and rim; can form aggregate interior or outermost facies where *pcA* or luf*A* not present.	*Inner*: Gradational and sub-spherical from *pcA* or *pA*. *Outer:* Sharp or gradational into *pA*; gradational into luf*A*; outer boundary is undulating.	Porous fine ash [**pA**] As *mA* but with high network porosity; elongate particles >20µm show a weak fabric; occurs as lenses or layers on the exterior of *mA*; contact with *mA* is undulating and both gradational or sharp along the same horizon.
	Laminated ultrafine ash [**lufA**] Medium to well sorted ultra-fine ash with a tightly packed, laminated framework; fines outwards; elongate particles typically aligned parallel to laminations; lamina are <100 µm thick and defined by variations in porosity as a function of grainsize; infills topography of mA/pA surface; porosity is ~13%; typical facies thickness ~0.7 mm; max. particle length ~0.35 mm; M_z ~20 µm; σ_i ~1 phi; forms <15% of aggregate radius.	Forms exterior rims of most aggregates; rarely present as a concentric layer within an aggregate.	*Inner:* commonly gradational from *pcA*, *mA* or *pA*. *Outer:* Sub-spherical, sharp.	

Table 1. Summary description of facies and representative SEM images from accretionary lapilli examined from the Tierra Blanca Joven deposits.